nature astronomy

Article

https://doi.org/10.1038/s41550-024-02238-3

Orbital polarimetric tomography of a flare near the Sagittarius A* supermassive black hole

In the format provided by the authors and unedited

Orbital Polarimetric Tomography of a Flare Near the Sagittarius A* Supermassive Black Hole: Supplementary Material

Aviad Levis[1*], **Andrew A. Chael**[2], **Katherine L. Bouman**[1], **Maciek Wielgus**[3], **Pratul P. Srinivasan**[4]

[1]California Institute of Technology, Pasadena, CA, USA.
[2]Princeton Gravity Initiative, Princeton University, Princeton, NJ, USA.
[3]Max-Planck-Institut für Radioastronomie, Bonn, Germany.
[4]Google Research, San Francisco, CA, USA.

In this work, we formulate a novel approach for estimating an evolving 3D structure around a black hole from light curve observations. To solve a tomography from a single viewpoint, we rely on both radiative emission and gravitational physics around the black hole. Integrating these physical models with a neural representation of the unknown 3D structure enables solving a highly ill-posed inverse problem, which we term *orbital polarimetric tomography*. By scanning over a range of possible inclination angles, we jointly estimate the inclination angle and 3D structure that best fit the polarimetric light curve data. Supplementary Fig. 1 shows an overview of the data-fitting procedure.

In the supplementary material we a) detail our evaluation of the orbital polarimetric tomography on synthetic simulations and b) add additional details and context for the general relativistic ray tracing. The organization is as follows: Sec 1 describes the data generation, Sec. 2 analyses the recovery results, and Sec. 3 covers additional details for general relativistic ray tracing, not included in the main text.

1 Synthetic data generation

To quantitatively assess our approach and the ability to recover the 3D structures and constrain an unknown inclination angle we generate synthetic data mimicking ALMA observations. Synthetic simulations allow for careful control of the sources of variability to evaluate the overall impact on the recovery performance. Each dataset consists of a flare on top of a background accretion disk as described in the following sections.

1.1 Emission flares

We generate data consisting of three distributions of emission: `Simple Hotspot`, `Flux Tube`, `Double Source` (Supplementary Fig. 2). Each volume spans a $40 \times 40 \times 40$ $[\mathrm{M}^3]$ cube with emission occupying an equatorial disk of $\sim 4 - 6M$ thickness. For these simulations, we assume a non-spinning black hole with a constant vertical magnetic field $\mathbf{B}(\mathbf{x}) = \hat{\mathbf{z}}B_z$. We model flares with high fractional polarization resulting in average fluxes matching the real ALMA data [1]

$$\bar{I}_I \simeq 0.3 - 0.4 \text{ Jy}, \tag{1}$$

$$\bar{P} = \sqrt{I_Q^2 + I_U^2} \simeq 0.1 - 0.15 \text{ Jy}. \tag{2}$$

Image frames and subsequent light curves are computed by discretizing an FOV of $40M$ ($\sim$200μas for Sgr A*) into 64×64 pixels. To reduce aliasing, each pixel value is computed by ray-tracing and averaging 10 sub-pixel rays, sampled uniformly within the pixel fov. For each 3D structure, observations are generated at two inclination angles: $\theta_{\mathrm{o}}^{\mathrm{lo}} = 12^\circ$ and $\theta_{\mathrm{o}}^{\mathrm{hi}} = 64^\circ$ resulting in a dataset of six polarimetric light curve observations. Supplementary Fig. 2 shows the 3D geometry and a sample of ray traced frames.

Based on our analysis of the validation-χ^2 for different initial times around 9:20 UT, we set the initial time of the flare to 9:20 UT, where the χ^2 of the ALMA data-fitting is lowest (Supplementary Fig. 3). For each simulated emission structure, we synthesize ~ 100 minutes of observations to mimic the time-averaged ALMA observations. We use a sampling cadence of ~ 1 data point per minute with appropriate scan gaps taken from the observational data.

To produce fluxes that are comparable to ALMA observed fluxes, we adjust the magnitude of the 3D emission structure and the volumetric LP fraction to satisfy Eqs. (1)–(2). We use a $q_f = 0.85$ to generate observations at $\theta_{\mathrm{o}}^{\mathrm{lo}}$ and $q_f = 0.5$ for $\theta_{\mathrm{o}}^{\mathrm{hi}}$; A lower q_f is used at a high inclination to account for the stronger Doppler boosting.

1.2 Accretion disk

While ALMA observations have low instrumental noise (~ 2 orders of magnitude less than the signal), a significant source

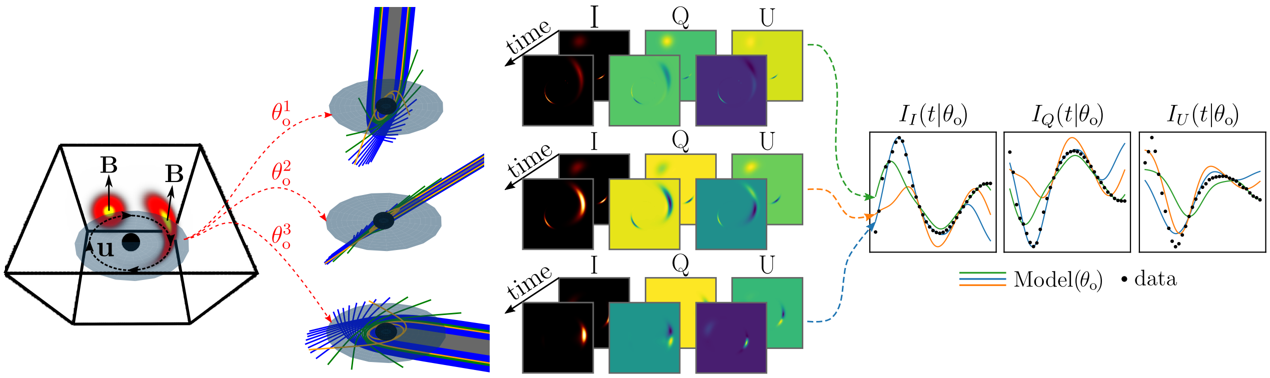

Supplementary Fig. 1. Illustration of the simultaneous estimation of 3D emission and inclination angle from polarimetric lightcurve data. The light curves (I_I, I_Q, I_U) depend on the unknown inclination angle (θ_o) which gives rise to a different image-plane and subsequently model fit. From left to right: 1. An emission bright spot with azimuthal velocity $\mathbf{u}$ orbits a black hole on the equatorial plane. The vertical magnetic field $\mathbf{B}$ induces polarized synchrotron radiation. 2. Geodesic curves are computed for every pixel at each inclination angle. 3. Integrating emission along geodesics to generate a Stokes image plane over time. 4. Summing over image pixels gives the model prediction per inclination angle.

of systematic noise is the unaccounted-for variability of the background accretion disk. To assess the impact the background signal has on reconstructions we generate synthetic data of a dynamic accretion disk. We model the accretion disk as a stochastic flow designed to mimic the statistics around Sgr A* [2, 3]. The 2D spiral flow is generated as a Gaussian Random Field (GRF) [4] which is inflated to 3D through convolution with a 1D vertical Gaussian kernel with a full-width half max (FWHM) of 2.35M. Subsequently, the 3D flow is gravitationally lensed (with the same ray-tracing procedure described for the foreground emission flares) to generate a polarized image plane. Supplementary Fig. 4 illustrates the 3D evolution of a randomly sampled `Accretion Disk` alongside the `Simple Hotspot`. Furthermore, the image plane containing both components is shown at two different evolution times.

2 Synthetic data recovery

In this section, we study the recovery performance through experiments designed to highlight different aspects of the tomography approach. In all recoveries, the 3D structure is visualized by sampling the network on a 3D grid at a resolution of ~ 0.15M. The visualized volumes are in-fact the estimated intrinsic 3D emission (without spacetime curvature).

2.1 Estimating inclination

Using the `Simple Hotspot` model with background accretion noise (σ_P) we show how the conditional $\chi^2(\theta_o|\mathbf{w}^\star)$ enables differentiating θ_o^{lo} from θ_o^{hi} (Supplementary Fig. 5). The right panel of Supplementary Fig. 5 highlights the overfitting gap, illustrating how low inclination angles are prone to overfitting. Intuitively, this is because a high inclination provides a stronger physical constraint, requiring the 3D emission to "disappear" behind the black hole for parts of the orbit. Nevertheless, the validation curves mitigate overfitting and enable estimating $\theta_o^\star$ (as the global minimum) to within $\pm 10°$ of the underlying true inclination. This is because overfit structures do not generalize as well and are less stable under perturbations to pixel positions on the image plane.

2.2 Sensitivity to background noise

In reality, observed variability is due to both the flare and accretion, however, it is difficult to determine the relative contributions of each source. Any un-modeled accretion dynamics will impact recovery results as our model fully attributes dynamics to orbital motion. We explore this aspect by sampling random fields that mimic an accretion process with varying degree of polarization ($q_f = \{0.25, 0.5, 0.75\}$ Jy) producing noise light curves with $\sigma_P = \{0.01, 0.03, 0.06\}$ Jy. Similar to the pre-processing of ALMA data [1], we subtract the time-averaged LP component (the static component of the background emission). A comparison between the simulated `Simple Hotspot` flare and accretion disk light curves, for different levels of variability, is shown in Supplementary Fig. 6 (top panels). In these simulations, the underlying true inclination is θ_o^{lo}. For each level of noise, σ_P, we are able to estimate $\theta_o^\star$ to within $\pm 4°$ of the true value.

using the validation-χ^2 minimum, our approach is able to recover the inclination angle to within $\pm 4°$ of the true value (see χ^2 curves at the bottom of Supplementary Fig. 6). Subsequently, using the estimate $\theta_o^\star$, we recover the unknown 3D emission. Supplementary Fig. 6 (middle row) shows a comparison between the recovered 3D emission and the ground truth. As the unaccounted disk variability increases, more emission is attributed sporadically within the volume. Nevertheless, the compact hotspot remains the brightest feature in the recovered 3D volume centered around the true azimuthal position.

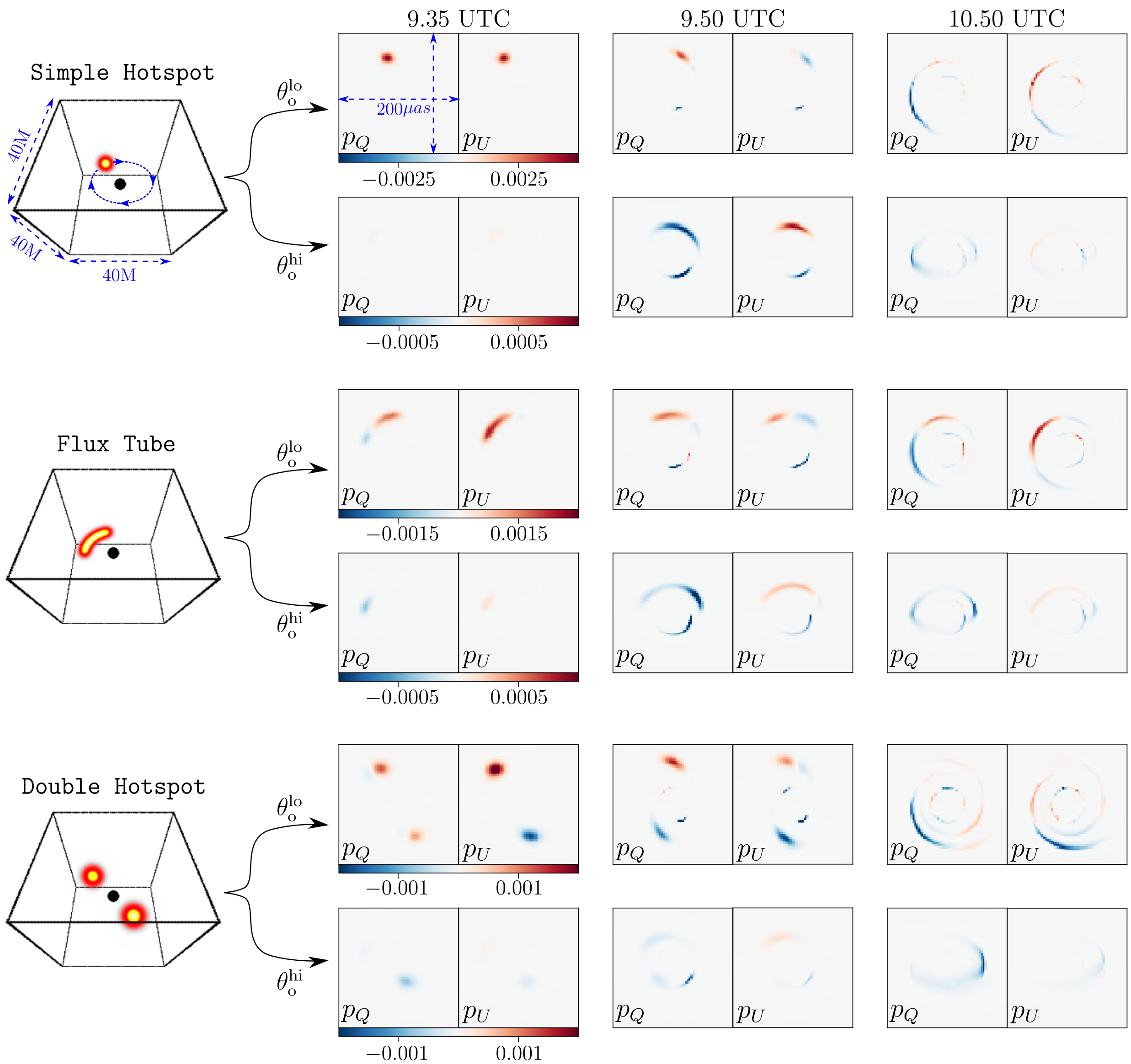

Supplementary Fig. 2. Synthetic simulations of three emission structures: `Simple Hotspot`, `Flux Tube`, `Double Source`. Observations are generated at two inclination angles: $\theta_o^{lo} = 12°$, $\theta_o^{hi} = 64°$. This figure illustrates the gravitationally lensed LP images: p_Q, p_U at three times within a period mimicking the *radio-loops* observed by ALMA: 9.35 – 11 UTC (April 11, 2017). Images are computed at FOV $= 40M$ ($\sim 200\mu$as for Sgr A*) discretized into 64×64 pixels. To reduce aliasing effects, each pixel is computed as an average of 10 randomly sampled sub-pixel rays. All models share the same dimensions and orbit highlighted in blue for the `Simple Hotspot`. Note the secondary images formed by gravitational lensing, evident in the `Simple Hotspot` and `Flux Tube` models (the bottom half of the image plane at 9.50 UTC)

2.3 Recovering different 3D morphology

In these simulations, we highlight the tomographic ability to recover different underlying emission structures and distinguish between different 3D flare morphologies.

For each of the datasets we add accretion disk noise with $\sigma_P = 0.01$ Jy and estimate the inclination angle, $\theta_o^\star$ as the minimum in the validation-χ^2 (curves are given in Supplementary Fig. 7). Our approach is able to estimate θ_o^{lo} to within $\pm 6°$ for all three levels of accretion noise and 3D fiducial datasets. While low and moderate accretion noise enable detection θ_o^{hi} to within $\pm 16°$, it is difficult to estimate θ_o^{hi} under high accretion noise. Nonetheless, even with high accretion noise, the trends of the validation-χ^2 curves enable a robust binary detection of low vs high inclinations.

Supplementary Fig. 8 highlights how our approach is able to simultaneously estimate an unknown inclination and 3D structure from unresolved light curve observations. In each case, the recovered 3D captures the unique morphology of

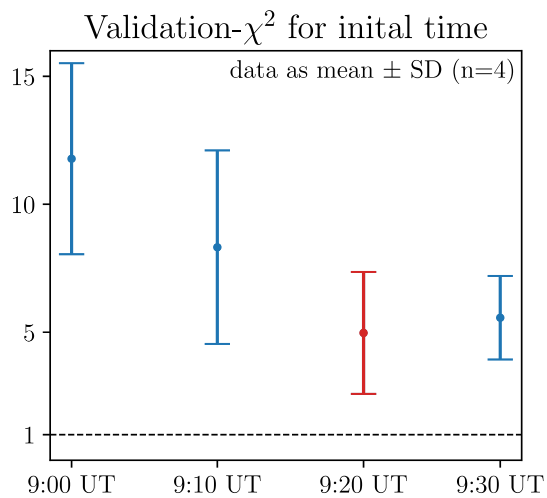

Supplementary Fig. 3. Validation-χ^2 for different initial times around the 9:20 UT. The best data-fit (lowest validation-χ^2) is highlighted in red. The error bars for each initial time are computed by recovering the 3D structure with four random initializations.

the underlying ground truth structure and is smoothed out by the tomographic reconstruction process.

It is instructive to visualize noise present in the 3D reconstructions. To illustrate noisy features we recover the 3D volume of a stochastic disk, without an orbiting bright flare, from light curve observations. In these recoveries the dynamic signal does not conform to the model assumptions made by the orbital tomography algorithm as brightness does not merely orbit and shear but also appears and disappears. Supplementary Fig. 9 demonstrates the 3D reconstructions with different random seeds (initial conditions for the neural network / 3D volume). Under certain initializations compact emission may appear, however, in contrast to the reconstructions of flares, these components are not stable. The consistent artifacts at the boundary, also present in the real data reconstructions (Figs. 1, 4 of the main text), suggest these are likely an artifact of the reconstruction algorithm.

2.4 Recovery blind spot

Close to the event horizon, gas is orbiting at relativistic velocities resulting in a substantial Doppler boosting effect, Doppler boosting effects are particularly strong at high inclination angles where emission moving away appears very faint compared to emission moving towards the observer. This is clearly illustrated in Supplementary Fig. 2 where one of the bright spots in the `Double Source` images is extremely faint due to the clockwise rotational motion. For this reason, we anticipate that reconstruction errors will not be distributed equally across the orbital plane.

To test this hypothesis we simulate observations with two sources, one at a fixed `11 o'clock` azimuthal position and the other at variable `2/4/8 o'clock` positions (Supplementary Fig. 10). The recoveries shown in Supplementary Fig. 10 reveal an "invisible region" at high inclination angles where sources are dim due to Doppler boosting. Due to recovery blurring, bright features that are close together merge to form a single region (see `2/4/8 o'clock` positions in Supplementary Fig. 10). Nevertheless, these regions contain two distinct brightness peaks attributed to the two hotspots. Doppler boosting is weaker at low inclination angles which are favored by the real data fit.

3 General Relativistic Ray Tracing

This section describes the General Relativistic (GR) equations used to compute geodesic paths and polarized radiative transfer.

3.1 Kerr metric

We work in the Kerr black hole spacetime in units where $G = c = 1$. A Kerr black hole has mass M and spin a. We use Boyer-Lindquist coordinates, where points in the spacetime are indicated by a four-vector $x^\mu = (t, r, \theta, \phi)$.

The structure of spacetime is encoded in the metric $g_{\mu\nu}$, which is a 4×4 symmetric matrix. In Boyer-Lindquist coordinates, the nonzero components of the metric are

$$g_{tt} = -(1 - 2Mr/\Sigma) \tag{3}$$
$$g_{rr} = \Sigma/\Delta \tag{4}$$
$$g_{\theta\theta} = \Sigma \tag{5}$$
$$g_{\phi\phi} = \Pi \sin^2\theta/\Sigma \tag{6}$$
$$g_{t\phi} = g_{\phi t} = -2Mar\sin^2\theta/\Sigma. \tag{7}$$

where the following are commonly used abbreviations.

$$\Delta = r^2 + a^2 - 2Mr \tag{8}$$
$$\Sigma = r^2 + a^2\cos^2\theta \tag{9}$$
$$\Pi = (r^2 + a^2)^2 - a^2\Delta\sin^2\theta \tag{10}$$
$$\omega = 2aMr/\Pi. \tag{11}$$

The nonzero components of the inverse metric $g^{\mu\nu}$ are

$$g^{tt} = -\Pi/\Delta\Sigma \tag{12}$$
$$g^{rr} = \Delta/\Sigma \tag{13}$$
$$g^{\theta\theta} = 1/\Sigma \tag{14}$$
$$g^{\phi\phi} = (\Delta - a^2\sin^2\theta)/(\Delta\Sigma\sin^2\theta) \tag{15}$$
$$g^{t\phi} = g^{\phi t} = -2Mar/\Delta\Sigma. \tag{16}$$

3.2 Ray tracing

We define the image plane of the observer at time $t = 0$, at radius $r_o \to \infty$, and at an inclination angle θ_o to the angular momentum axis of the black hole (BH). We use Cartesian coordinates (α, β) on the image plane, measured in units of M. Restoring physical units, the image plane coordinates are in radians with the scale given by GM/Dc^2 where D is the distance to the BH. Time is measured in units of GM/c^3. The origin $\alpha = \beta = 0$ is the line of sight to the black hole

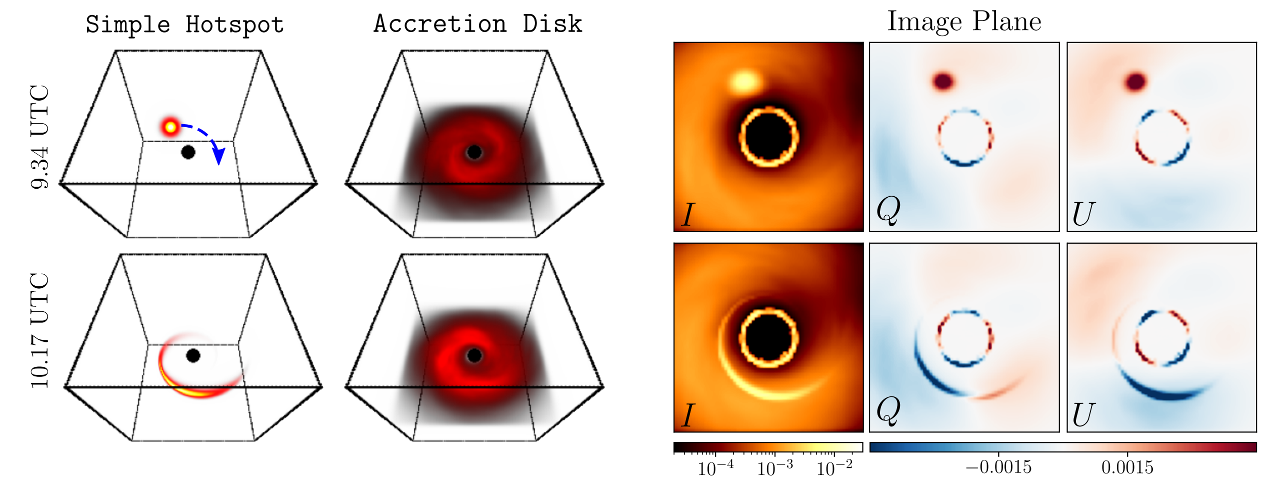

Supplementary Fig. 4. An illustration of the `Simple Hotspot` and `Accretion Disk` used for background noise. [left panels] Evolving 3D emission at three different times (rows). [right panels] Corresponding image frames ray-traced for a non-spinning black hole at a low inclination angle (θ_o^{lo}). The bright ring is caused by gravitational lensing of the accretion disk with a diameter of $\sim 50\ \mu$as consistent with the images of Sgr A* [5].

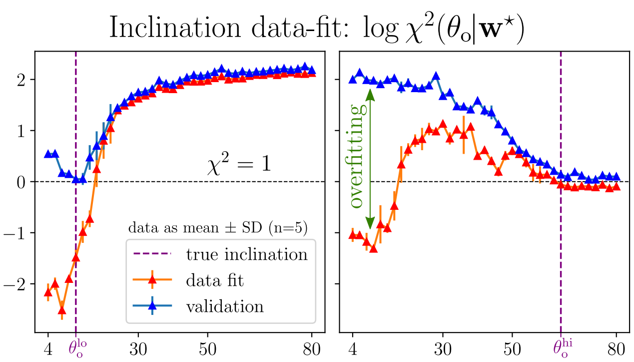

Supplementary Fig. 5. Inclination vs validation χ^2 highlighting the role of the validation χ^2 in model selection. The χ^2 plots are for a `Simple Hotspot` flare with background accretion noise: $\sigma_P = 0.01$. The left/right panels show the χ^2 for the true low/high inclinations. The right panel shows how even when the true inclination is θ_o^{hi}, low inclination angles are prone to overfitting the data. The validation χ^2 mitigates over-fitting and enables estimating the underlying inclination angle as the global minimum. For each angle, the 3D recovery is run with five random initializations with error bars indicating the recovery stability.

at $r = 0$, and the $+\beta$ image plane axis is parallel with the BH spin direction (i.e. with the $-\theta$ direction).

We solve for the trajectories of photons backward from a specific position (α, β) on the image plane using a set of differential equations which in Einstein notation can be written as:

$$\frac{dx^\mu}{d\sigma} = k^\mu. \tag{17}$$

Here σ is the path parameter ("affine time") and

$$x^\mu(\sigma) = (t(\sigma), r(\sigma), \theta(\sigma), \phi(\sigma)), \tag{18}$$

is a parameterized trajectory in spherical (Boyer-Lindquist) coordinates.

Each photon trajectory is defined by three *constants of motion*: (E, λ, η). E is photon energy at infinity (i.e., observed frequency). The parameters λ (angular momentum) and η (Carter constant) are fully determined by the photon's coordinates on the observer screen:

$$\lambda = -\alpha \sin\theta_o \tag{19}$$
$$\eta = (\alpha^2 - a^2)\cos^2\theta_o + \beta^2. \tag{20}$$

From these constants, at each point along the trajectory, the photon's *covariant momentum* (lower index) k_μ is given by [6]:

$$k_t = -E \tag{21}$$
$$k_r = \pm E\sqrt{\mathcal{R}(r)}/\Delta \tag{22}$$
$$k_\theta = \pm E\sqrt{\Theta(\theta)} \tag{23}$$
$$k_\phi = E\lambda, \tag{24}$$

where $\mathcal{R}$ and Θ are *radial and polar potentials*:

$$\mathcal{R}(r) = (r^2 + a^2 - a\lambda)^2 - \Delta\left[\eta + (\lambda - a)^2\right] \tag{25}$$
$$\Theta(\theta) = \eta + a^2\cos^2\theta - \lambda^2/\tan^2\theta. \tag{26}$$

The choice of $\pm$ sign in Eq (21–24) depends on the direction of motion (signs reverse at angular and radial turning points when $k^\theta = 0$ or $k^r = 0$, respectively.).

Equation (17) is described in terms of the *contravariant* (upper index) momentum vector k^μ, which is obtained by multiplying the *covariant* momentum (Eqs. 21–24) by the inverse metric

$$k^\mu = g^{\mu\nu}k_\nu. \tag{27}$$

To compute geodesic paths $x^\mu(\sigma)$, we solve Eq. (17) using the explicit parametric form described by [6] and implemented in [7].

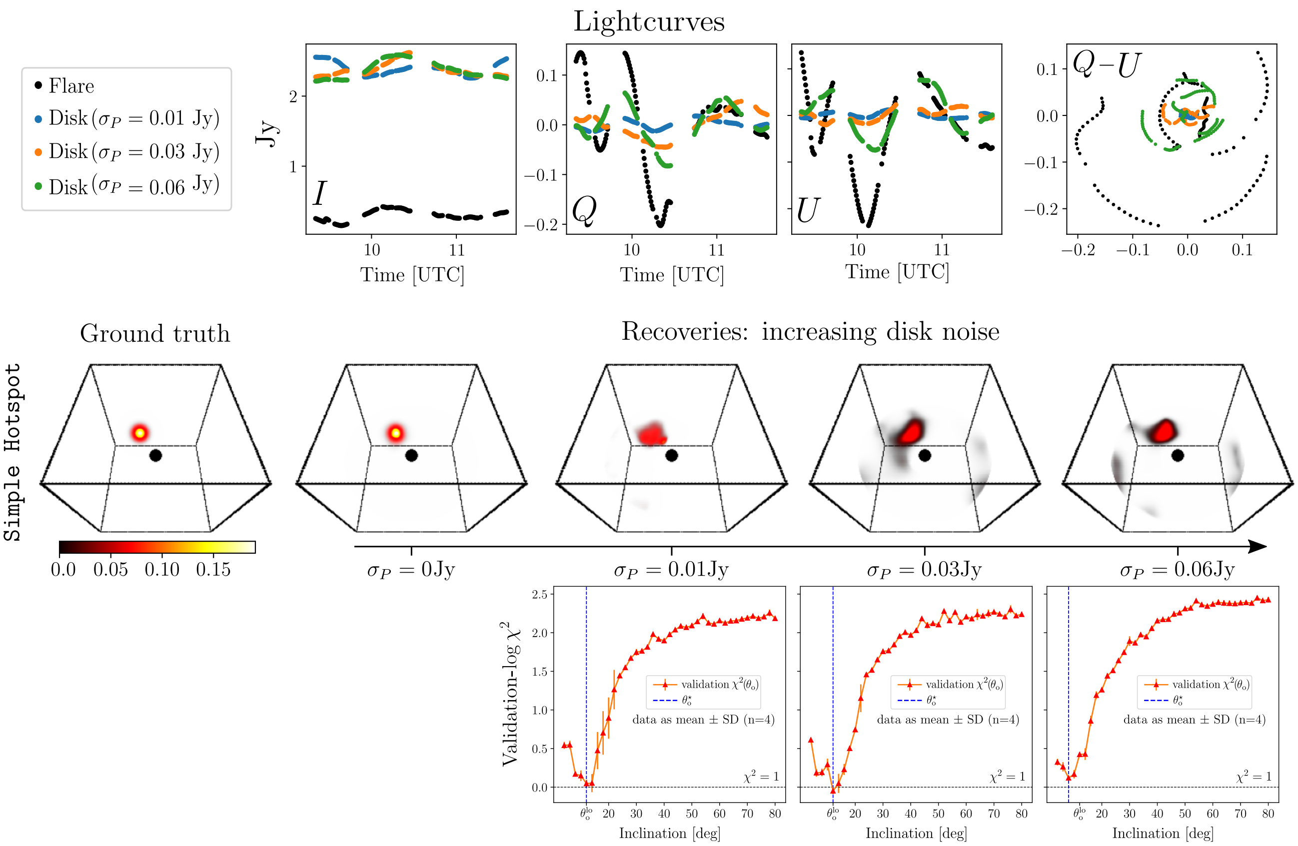

Supplementary Fig. 6. Analysis of the data and reconstructions for three levels of accretion variability. [Top] A comparison between the light curves of the foreground flare and background accretion disk for three levels of disk variability $\sigma_P = \{0.01, 0.03, 0.06\}$ Jy. [Middle] 3D reconstructions for the three levels of variability. These volumes represent the true/estimated initial emission at 9.35 UTC. The recovered 3D emission captures the compact underlying true flare structure, size and position. [Bottom] In all cases, the estimated inclination $\theta_o^\star$ (blue) (estimated as the global minimum) is within $\pm 4^\circ$ of the underlying true inclination $\theta_o^{\rm lo}$. The error bars are computed by running the 3D recovery with four random initializations.

3.3 Fluid Velocity and Redshift

Outside the ISCO, the four-velocity u^μ of prograde circular orbits in the equatorial plane is $u^\mu(r)$, where:

$$u^t = u^t \tag{28}$$
$$u^r = 0 \tag{29}$$
$$u^\theta = 0 \tag{30}$$
$$u^\phi = u^t\Omega, \tag{31}$$

Since the four-velocity must be normalized so that $u^\mu u_\mu = g_{\mu\nu}u^\mu u^\nu = -1$,

$$u^t = \frac{1}{\sqrt{-g_{tt} - 2\Omega g_{t\phi} - \Omega^2 g_{\phi\phi}}}. \tag{32}$$

The redshift factor g describes the change in frequency of a photon between the observer's frame at infinity and the frame where it is emitted.

$$g^{-1} = \frac{\nu_{\rm emis}}{\nu_{\rm obs}} = \frac{-k_\mu u^\mu}{E}. \tag{33}$$

3.4 Parallel transport

Ray-tracing polarization in curved spacetime requires parallel transport of the emitted polarization to the observer screen. We define this operation as a rotation matrix: $\mathbf{R}$ (main text: Eq. 5). This matrix multiplies the emission-frame Stokes vector $\mathbf{J}$ to rotate the linearly polarized components:

$$\mathbf{RJ} = \begin{bmatrix} 1 & 0 & 0 & 0 \\ 0 & \cos 2\chi & -\sin 2\chi & 0 \\ 0 & \sin 2\chi & \cos 2\chi & 0 \\ 0 & 0 & 0 & 1 \end{bmatrix} \begin{bmatrix} J_I \\ J_Q \\ 0 \\ J_V \end{bmatrix}. \tag{34}$$

The angle χ at pixel coordinates (α, β) is given by [8]:

$$e^{2i\chi} = \frac{(\beta + i\mu)(\kappa_1 - i\kappa_2)}{(\beta - i\mu)(\kappa_1 + i\kappa_2)}, \tag{35}$$

where $\kappa = \kappa_1 + i\kappa_2$ is the complex Penrose-Walker constant, a quantity that is computed in the emission frame and then conserved in parallel transport, and $\mu = -(\alpha + a\sin\theta_o)$.

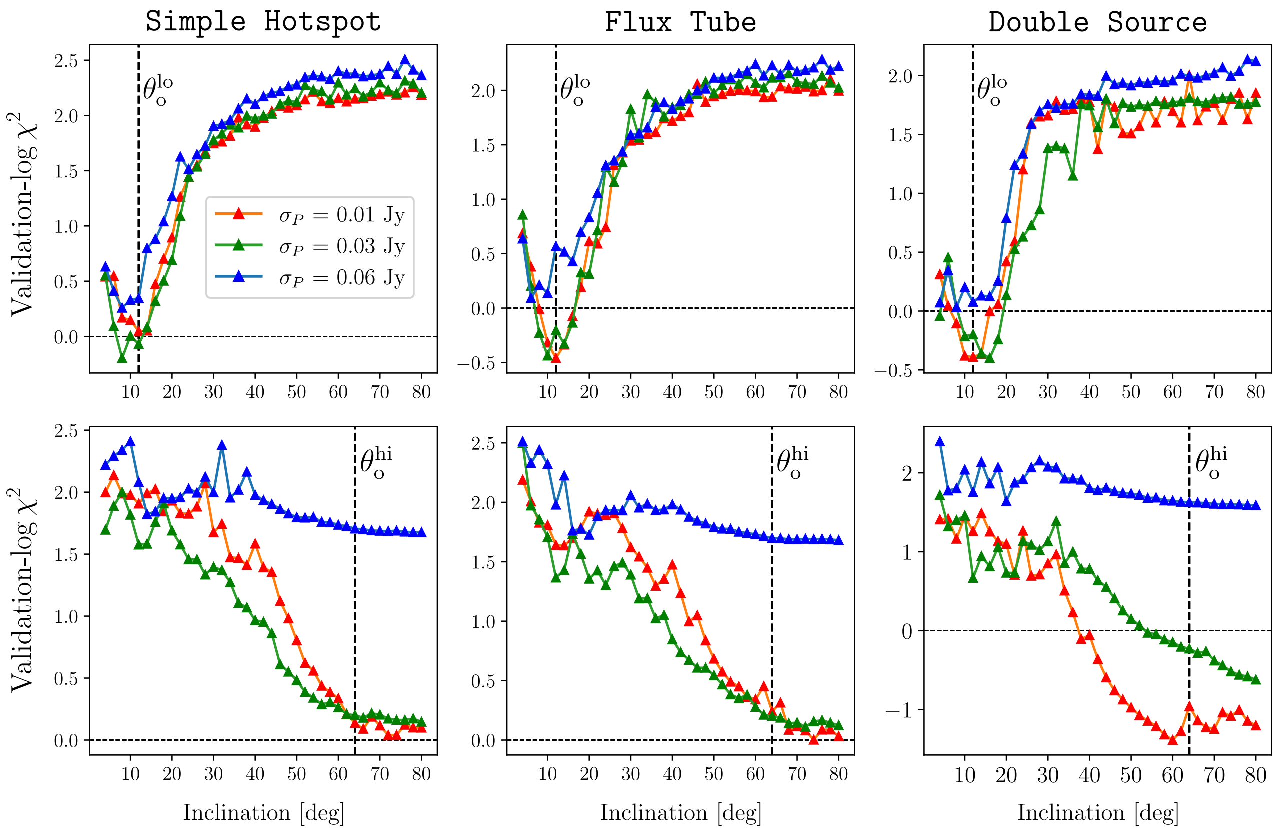

Supplementary Fig. 7. Validation-χ^2 for three synthetic emission structures (Supplementary Fig. 2) under two true inclination angles ($\theta_o^{lo}/\theta_o^{hi}$) and three levels of accretion variability (σ_P). The red curves correspond to the estimated volumes shown in Supplementary Fig. 8. For θ_o^{lo} (top row), the minimum is within $\pm 6°$ of the true inclination for all noise levels and exactly coincides with the true inclination for low levels of noise (red curves). For θ_o^{hi} the minimum is within $\pm 16°$ of the true inclination for $\sigma_P = 0.01, 0.03$ Jy. While it is difficult to estimate the exact inclination under high accretion variability and inclination angle (bottom row, blue curves), the curve trends enable the detection of high vs low inclinations (compare blue curves at the top and bottom panels).

To compute κ in the emitter frame we first convert the coordinate-frame 4-vectors k^μ and b^μ for the magnetic field to local 3-vectors $\mathbf{k}$ and $\mathbf{B}$ using the tetrad matrices e_a^μ (which depend on the emission position and fluid velocity) as described in [9] (Equations 36-42). We then compute the local emitted polarization vector $\mathbf{f}$ from

$$\mathbf{f} = \frac{\mathbf{k} \times \mathbf{B}}{|\mathbf{k}|}. \tag{36}$$

We then convert $\mathbf{f}$ to a coordinate frame four-vector f^μ using the transpose tetrad matrix. The constant κ is then [9, 10]

$$\kappa = \kappa_1 + i\kappa_2 = (r - ia\cos\theta)(A - iB) \tag{37}$$

$$A = (k^t f^r - k^r f^t) + a\sin^2\theta(k^r f^\phi - k^\phi f^r) \tag{38}$$

$$B = \left[(r^2 + a^2)(k^\phi f^\theta - k^\theta f^\phi) - a(k^t f^\theta - k^\theta f^t)\right]\sin\theta. \tag{39}$$

References

[1] M. Wielgus, M. Moscibrodzka, J. Vos, Z. Gelles, I. Martí-Vidal, J. Farah, N. Marchili, C. Goddi, and H. Messias. Orbital motion near Sagittarius A* . Constraints from polarimetric ALMA observations. *Astron. Astrophys.*, 665:L6, 2022.

[2] Event Horizon Telescope Collaboration. First Sagittarius A* Event Horizon Telescope Results. III. Imaging of the Galactic Center Supermassive Black Hole. *Astrophys. J. Lett.*, 930(2):L14, 2022.

[3] A. Levis, D. Lee, J. A. Tropp, C. F. Gammie, and K. L. Bouman. Inference of Black Hole Fluid-Dynamics from Sparse Interferometric Measurements. In *Proc. IEEE/CVF Intl. Conf. Comput. Vision (ICCV)*, 2340–2349, 2021.

[4] D. Lee and C. F. Gammie. Disks as Inhomogeneous, Anisotropic Gaussian Random Fields. *Astrophys. J.*, 906(1):39, 2021.

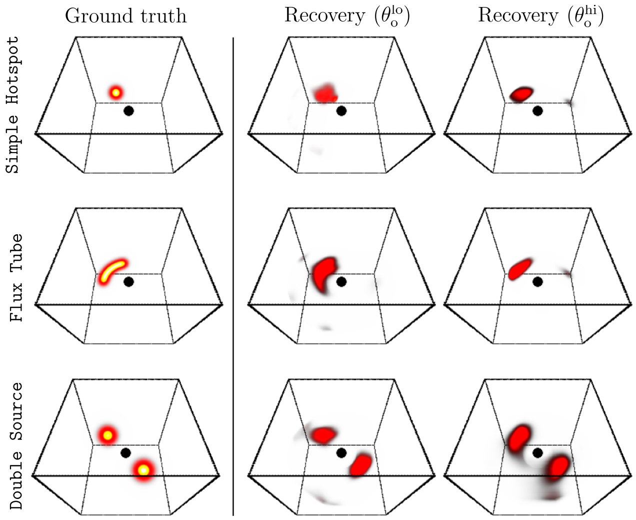

Supplementary Fig. 8. 3D recoveries for three simulated structures observed at two (unknown) inclination angles: $\theta_o^{lo} = 12°$, $\theta_o^{hi} = 64°$. Using synthetically generated light-curves as observations, the 3D reconstructions are able to reconstruct different flare morphologies in the presence of background accretion noise. The recovered structure is given under an inclination $\theta_o^\star$ that minimizes the validation-χ^2 (Fig. 7). Note: this figure is a replica of Fig. 6 in the main text, shown here for convenience.

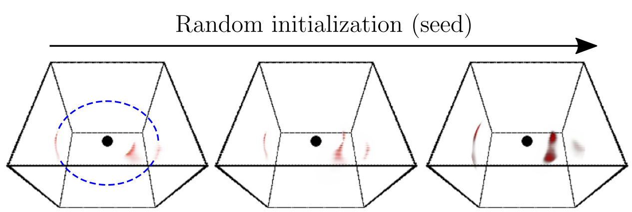

Supplementary Fig. 9. 3D reconstruction of a stochastic accretion disk (Supplementary Fig. 4) without an orbiting bright flare. In these recoveries the observed dynamic signal does not follow the assumptions of orbital tomography. Different initializations (seeds) lead to different local minima. Visualizing the converged solutions gives a sense of the artifacts that would appear in a real data reconstruction (the color bar matches Supplementary Fig. 6) The domain boundary is highlighted in blue in the leftmost recovery.

[5] Event Horizon Telescope Collaboration. First Sagittarius A* Event Horizon Telescope Results. I. The Shadow of the Supermassive Black Hole in the Center of the Milky Way. *Astrophys. J. Lett.*, 930(2):L12, 2022.

[6] S. E. Gralla and A. Lupsasca. Null geodesics of the Kerr exterior. *Phys. Rev. D*, 101(4):044032, 2020.

[7] A Chael. kgeo (version 1.0.0). `https://github.com/achael/kgeo`, 2023. Online; accessed 01-June-2023.

[8] E. Himwich, M. D. Johnson, A. Lupsasca, and A. Strominger. Universal polarimetric signatures of the black

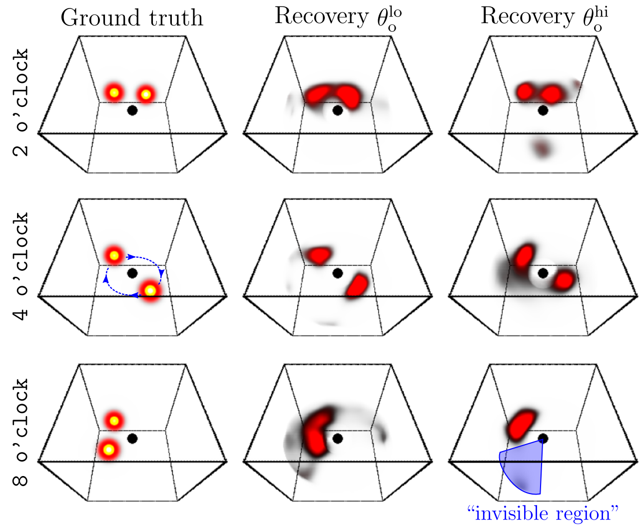

Supplementary Fig. 10. 3D recoveries of two bright spots in a clockwise orbit highlight the effects of Doppler boosting. The initial position of one source is fixed `11 o'clock` and the other at `2/4/8 o'clock` (different rows). Each column represents recoveries with observations at a different inclination angle $\theta_o^{lo}/\theta_o^{hi}$. Doppler boosting acts to dim sources moving away from the observer resulting in a blind spot (highlighted in blue) at high inclination angles. Nevertheless, for the `2/4 o'clock` orbital configurations our approach is able to recover the distinct structure of two emission sources.

hole photon ring. *Phys. Rev. D*, 101(8):084020, 2020.

[9] J. Dexter. A public code for general relativistic, polarised radiative transfer around spinning black holes. *Mon. Not. R. Astron. Soc.*, 462(1):115–136, 2016.

[10] Z. Gelles, E. Himwich, M. D. Johnson, and D. C. M. Palumbo. Polarized image of equatorial emission in the Kerr geometry. *Phys. Rev. D*, 104(4):044060, 2021.